JOURNAL OF COMPUTATIONAL PHYSICS 121, 331–346 (1995)

Simulation of the Quasi-Static Mechanics and Scalar Transport Properties of Ideal Granular Assemblages

X. ZHUANG, A. K. DIDWANIA, AND J. D. GODDARD

Department of Applied Mechanics and Engineering Sciences, University of California, San Diego, La Jolla, California 92093-0411

Received February 7, 1994; revised March 27, 1995

The current article reports on the further development of a new technique for the computer simulation of the quasi-static mechanics and scalar transport properties of sphere assemblages. In an extension of a previous 2D simulation to 3D, we have developed an improved computation based on several innovations: a shuffling algorithm to rapidly generate random loose-packed configurations of particles; a microcell-adjacency method to accelerate particle-contact search; a relaxation method to overcome singularities in the static transport equations; and a simulated mechanical compression to generate dense random initial states. The improved algorithm allows for 3D simulations on a workstation platform. As major results, the dilatancy (volume expansion) computed for random dense-packed assemblages is found to depend on interparticle friction, contrary to the classical Reynolds hypothesis. Also, the use of linear-elastic contacts is found to be valid near the rigid-particle limit of interest here. Experimental data from ("triaxial" compression) tests agree well with the simulations of both the shear strength and the electrical conductivity of sphere assemblages, when proper account is taken of the actual electrical contact resistance between steel balls as a function of load. One major conclusion is that scalar transport can serve as a useful macroscopic probe of particle-contact topology in granular media.

I. INTRODUCTION

Granular media are materials composed of distinct, independently mobile particles which interact only at localized interparticle contacts. Because of the analytical intractability, computer simulation has become a widely accepted method for theoretical study of the mechanics. As in other branches of multibody physics, such simulation allows one to extract any desired microscopic information at any stage of a computation, and "experiments" can be performed numerically that would be virtually impossible physically. Many previous works show, moreover, that numerical simulations can describe qualitatively the overall continuum mechanical behavior of real granular materials [20, 21, 50, 51, 18], although current numerical studies have not progressed much beyond idealized particle shapes such as the disks and spheres, considered here, or ellipsoids. Also, while the number of particles is small compared to real granular systems such as sand masses, sample-size effects are partly overcome by the use of periodic-cell models. As in other branches of physics, it is not unreasonable to hope that certain universal aspects of the collective behaviour of large assemblages can be captured by simulations on relatively small assemblages and simple particle shapes. In any event, this appears to us a compelling first step in understanding more complex systems.

We recall that the behavior of granular media depends generally on a variety of factors, such as particle volume fraction or "void ratio," interparticle friction, particle shape, and microstructural contact topology or "fabric," to name the most prominent. While granular fabric is believed to be one of the most important factors determining the overall mechanical response to deformation, the direct measurement of fabric in real granular materials such as sand [41, 42] is difficult and tedious. It would, therefore, be highly desirable to ascertain whether fabric can be related to or inferred from measurements of other macroscopic properties. Indeed, dynamic shear moduli and the corresponding set of elastic constants obtained from wave-speed measurement are found to contain such information [15, 31, 1].

Apart from various mechanical properties, it is plausible, based on experience with the optical and transport properties of other materials, that a scalar transport property such as electrical or thermal conduction, can provide yet another macroscopic indicator of fabric. The effective conductivity of granular materials depends not only on the conductivities of solid grains and any interstitial (or "pore") fluid, but also on void ratio and fabric. Attempts have already been made to study the evolution of mechanical anisotropy of water saturated sands and clays by monitoring electrical conductivity [38, 6, 3, 4]. However, since sand grains or soil particles are themselves not electrically conductive, the current must be conducted by the pore water, so that conductive anisotropy mainly reflects void-space geometry. While the latter may reveal some aspects of internal structure, it does not serve as a particularly good indicator of granular-contact topology. In particular, the variation of interparticle forces in load-bearing chain structures is not captured by pore–fluid conductivity, a fact which provides much of the motivation for the present of conductivity simulations and experiments.

In Section VI, we derive an expression for the effective conductivity of idealized granular assemblages and we review

0021-9991/95 $12.00

the mean-field approximation proposed by Batchelor and O'Brien [10]. Numerical simulations, mainly aimed at the study of the microstructural properties are presented in Section VII, and the computer simulations are compared with experiment in Section VIII.

II. THE QUASI-STATIC METHOD

Currently, one can identify two main classes of numerical simulation for the mechanics of granular materials, namely, the *dynamic* and the *quasi-static.* The former, based on the full Newtonian equations of motion and referred to as the "distinct element method" (DEM) in the older literature, was first developed by Cundall and coworkers [20] and has been widely employed since [21, 50, 22, 51, 12, 16, 8]. However, various artificial damping procedures are usually employed in this method in order to suppress parasitic particle vibrations, an artifact which becomes particularly bothersome if one is ultimately interested only in quasi-static conditions. For this reason among others, direct quasi-static simulation has been receiving increased attention in recent years [46, 35, 17, 9, 27, 7], even though it too involves computational artifacts, as discussed below and in the previous work of Bashir and Goddard [9]. In contrast to the latter work, which involved supercomputer implementation of a 2D simulation, a major goal of the present effort was to develop a sufficiently efficient 3D simulation to run on widely available workstation platforms.

The present quasi-static simulation is based largely on an improved version of an earlier method [9], in which we recall that particle motions are determined as follows: given a small homogeneous incremental deformation imposed on an assemblage in a state of mechanical equilibrium, one first imparts to each particle a rotation and translation defined by the mean incremental deformation of the assemblage. This corresponds to the mean-field approximation of Jenkins and Strack [32], which leads to unbalanced elastic forces and torques. In the present algorithm, the assemblage is then restored to a new equilibrium configuration by means of incremental motions or "fluctuations" of each particle about the mean. Thus, unlike dynamic simulations, in which the full Newtonian dynamical equations are employed to update particle configurations, the fluctuating displacements of individual particles are determined *statically* by a global stiffness matrix and a system of equations,

$$\mathbf{Kx} = \mathbf{b}, \tag{1}$$

where $\mathbf{K}$ is the "grand stiffness matrix," $\mathbf{x}$ is the vector of the fluctuating translations and rotations of the particles, and $\mathbf{b}$ is the unbalanced force arising from the mean motion [9, 57]. The above procedure is repeated until the force and torque balances for each particle are satisfied to within some preset tolerance. The assemblage is allowed to expand or contract volumetrically to maintain a global control pressure or stress at some desired level, which thereby enables one to compute

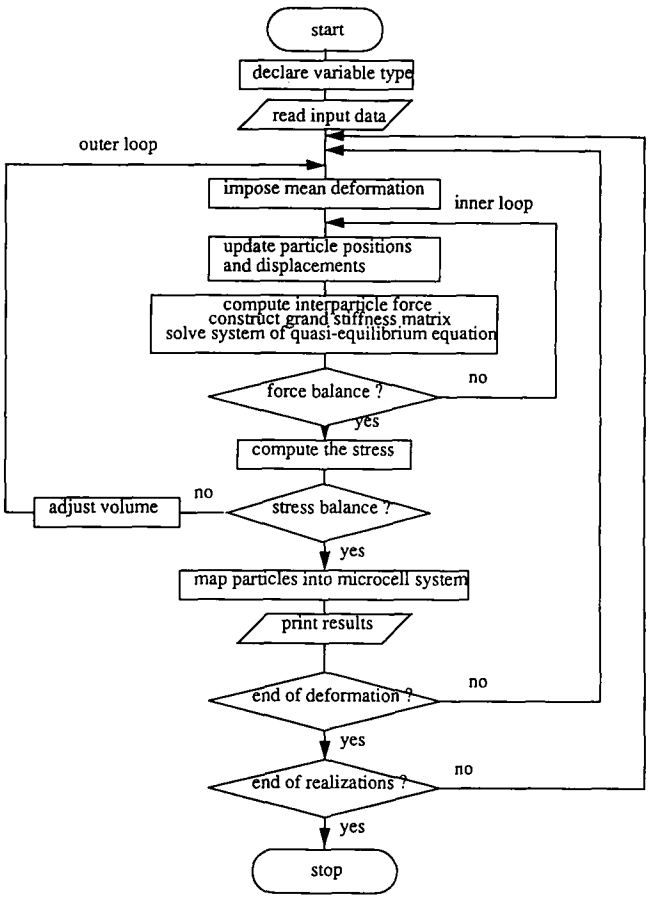

FIG. 1. Flowchart for the algorithm (solid fraction control used only in initial packing stage).

(Reynolds) dilatancy. Figure 1 presents a flowchart for the algorithm, and Appendix I summarizes the main equations and the computation of the stiffness matrix, which are extensions to 3D of the equations given by Bashir and Goddard [9]. A computer program listing is given by Zhuang [57].

At any stage of deformation, the stiffness matrix $\mathbf{K}$ is determined by the local contact stiffness between particles. Although various elastic contact models such as that of Hertz [26] lead to a nonlinear force–displacement relation for interparticle contacts, we mainly employ here a linear contact relation for the normal and tangential forces between particles. For our purposes, the contact elasticity serves to eliminate static indeterminacies in the idealized limit of rigid particles, which is of primary interest here. We shall, however, verify that the exact dependence of stiffness on contact force appears not to be of paramount importance. As in numerous previous works, the tangential slippage at contacts is assumed to be governed by Coulomb sliding friction [27, 57].

As pointed out in Ref. [5], the matrix $\mathbf{K}$ in (1) becomes singular whenever any cluster of particles loses contact with the remainder, giving rise to "neutral" or "zero-frequency"

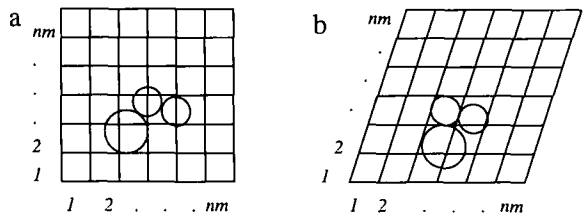

FIG. 2. Schematic of a periodic simulation cell and its microcells in (a) initial, and (b) sheared configurations.

elastic vibrational modes and a finite-dimensional null space for **K**. To overcome this singularity we utilize, as an improvement over Ref. [9], the classical relaxation method [48] as our linear-equation solver, which effectively yields a singular value decomposition to eliminate the zero-frequency modes. As discussed next, our computation also includes a "shuffling" algorithm for rapidly generating an initially random loose-packed configuration of particles and an improved microcell method to further accelerate particle-contact search [9, 27].

III. CONTACT DETECTION VIA MICROCELLS

To simulate pairwise interactions in a system of N particles, it is generally necessary to search for all particles within the range of spatial interaction of a given particle. In general, one needs $N(N-1)/2$ such searches, including a time-consuming evaluation of particle separations, a nontrivial task when the number of particles is large. However, the time spent on searching can be reduced to $O(N)$ by means of spatial microcells [2, 27] and the associated adjacency matrix.

In the 2D case, for instance, the deformable simulation cell is divided into regular lattice of $nm \times nm$ initially square microcells as shown in Fig. 2. A microcell is small enough to contain the center of at most one particle throughout the subsequent cellular deformations. All microcells are then labeled ordinally. For each microcell, the definition of adjacent microcells may include a neighborhood extending several microcell layers outward, depending upon the range of the pair interaction considered. Whatever the range, the adjacency of microcells is defined by a matrix Ac with elements:

$$\mathrm{Ac}(i,j) = \begin{cases} 1, & \text{if microcells } i \text{ and } j \text{ are adjacent} \\ 0, & \text{otherwise,} \end{cases}$$

where, $i, j = 1, 2, ..., n$ ($n = nm \times nm$), which is nothing more than the connectivity matrix of the associated graph [53]. We next define a second matrix Oc to represent the occupancy of microcells by particles:

$$\mathrm{Oc}(i,j) = \begin{cases} 1, & \text{if microcell } i \text{ is occupied by particle } j \\ 0, & \text{otherwise,} \end{cases}$$

where, $i = 1, 2, ..., n$, and $j = 1, 2, ..., N$. A third matrix Ap is then used to represent the adjacency of two particles:

$$\mathrm{Ap}(i,j) = \begin{cases} 1, & \text{if particles } i \text{ and } j \text{ are adjacent} \\ 0, & \text{otherwise,} \end{cases}$$

where, $i, j = 1, 2, ..., N$, as determined by their occupancy of adjacent or nonadjacent microcells. This matrix can be expressed as the matrix product:

$$\mathrm{Ap} = \mathrm{Oc}^{\mathrm{T}}\mathrm{AcOc}. \tag{2}$$

Once the microcell adjacency matrix Ac is established, it remains unchanged since the microcell topology is invariant under homogeneous deformation. Upon determination of the occupancy matrix Oc at each deformation step, the particle adjacency matrix Ap can be found easily by the simple operation (2). However, (2) is computationally equivalent to

$$\mathrm{Ap}(i,j) = \mathrm{Ac}(\mathrm{map}(i), \mathrm{map}(j)), \tag{3}$$

where *map* defines a mapping array whose element map(i) equals the ordinal number(1, 2, ..., n) of the microcell occupied by particle i and which, therefore, corresponds to the row vectors of Oc. The method appears substantially equivalent to the "cell-index/linked-list" method of molecular dynamics [2]. Based on the computed particle adjacency matrix Ap, the current program determines all particle contacts, which permits construction of the stiffness matrix and calculation of contact forces.

In our rigid-sphere simulations, the size of the cubical microcell is chosen such that its largest diagonal is always equal to the smallest particle diameter in the system to assure that not more than one particle simultaneously occupies a given microcell. Furthermore, the largest particle diameter defines the cutoff distance within which one must search for potential contacts with neighboring particles. For a 2D monodisperse disk assemblage, therefore, two surrounding layers will be sufficient to cover the cutoff distance, which means there are 24 microcells adjacent to each microcell.

At the start of a simulation the microcell adjacency matrix Ac is constructed and remains unaltered throughout the computation. At each deformation step, whenever particles move to new positions, the mapping array is updated, which is an inherently rapid process. For a given particle, we need only look in the neighboring 24 microcells surrounding its microcell to find the adjacent particles. In the worst case, 24 searches are required if all neighboring microcells are occupied. Therefore, $12N$ provides an upper-bound on the total searches necessary if we consider a pair of neighboring particles as one search.

In reality, the number of searches required depends upon the number of particles lying within the cutoff distance and, hence, upon the system density and configuration. In a 2D random

particle assemblage, the average number of searches is far less than 24 per particle. In fact, in the course of our computations, the average number of searches for each particle is found to be about six for random loose-packed, and 11 for random dense-packed monodisperse disk systems. Therefore, the total number of searches is approximately $3N$ and $5.5N$, respectively.

IV. GENERATION OF INITIAL RANDOM LOOSE PACKINGS

In the past 30 years or so, random monodisperse packings of disks and spheres have been studied extensively by both experimental and theoretical means, in part because they serve as useful models for a variety of amorphous materials such as molecular fluids and glasses, as well as for granular materials and porous media. Dense ordered packing, dense random packing, and loose random packing represent three important idealizations. The dense ordered packing for rigid spheres of equal radii (monodisperse) has a density equal to 0.7405 in 3D (FCC or HCP). Similarly, the density is equal to 0.9069 in 2D (triangular). For dense random packings, it is generally believed that the densities fall into a range 0.62 to 0.66 for 3D and 0.81 to 0.87 for 2D [13, 25, 33, 45, 55].

In a previous related study of 2D disk assemblages [9], two distinct algorithms were employed to generate two types of assemblages: imperfect triangular close-packed for the monodisperse assemblage, and pseudo-gravitational packing for the polydisperse. Recognizing the limitation of those algorithms in generating random isotropic configurations of arbitrary density, we have developed a new algorithm capable of densifying an initially random loose configuration to any feasible desired density by means of cyclic shear under isotropic confining pressure, as discussed in Section V below. (One could if desired add body forces such as gravity which we shall not consider here.) We discuss here the major steps in generating random loose packings.

A. *Shuffling*

For the purposes of various Monte Carlo simulations [2], there are many ways of realizing random sequences, the conventional one being the standard random-number generation (RNG). For the purpose of repeatedly generating random particle assemblages in a way which is faster than the (built-in) random number generator available to us, we have developed a different way of generating random sequences by means of a "card-shuffling" algorithm. The idea is to degrade the order of a given sequence by means of a certain number of "riffle" shuffles. In our algorithm, a variant of the riffle shuffle is used, wherein each shuffle consists of one random "cut" and "flip" and one interlacing shuffle [23].

It is possible to make fairly rigorous theoretical estimates based on Shannon's theorem which suggests, incidentally, that seven riffle shuffles are sufficient to randomize a deck of 52 cards [23]. With this information as a guideline, a shuffling algorithm was implemented for rerandomizing a given loose random packing [57]. In order to compare our shuffling algorithm with a (built-in) random-number generator, we have calculated the autocorrelation between the shuffled sequence of 50 numbers and an initial ordered sequence, as well as the autocorrelation between two random sequences obtained by the random number generator. Let $S(i)$ represent the elements, $i = 1, 2, \ldots, n$, of an n-member sequence; then, we employ as autocorrelation function between two such sequences S_1 and S_2 the formula

$$A = \frac{\sum_{i=1}^{n} \sin\left[\frac{2\pi}{n}\left(S_2(i) - \frac{1}{2}\right)\right] \sin\left[\frac{2\pi}{n}\left(S_1(i) - \frac{1}{2}\right)\right]}{\sum_{i=1}^{n} \sin^2\left[\frac{2\pi}{n}\left(S_1(i) - \frac{1}{2}\right)\right]} \quad (4)$$

which treats the sequences as cyclical.

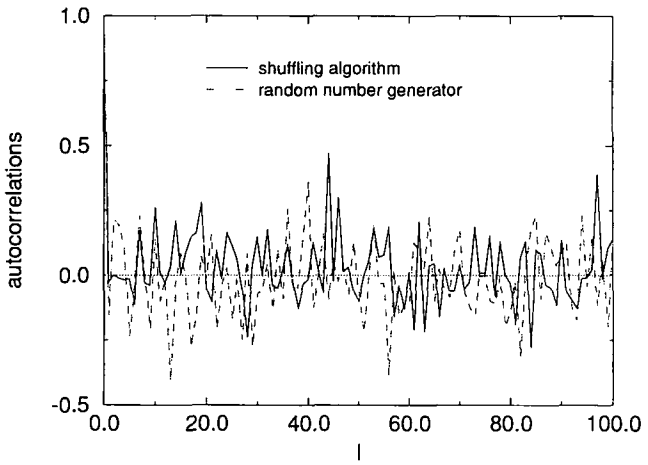

FIG. 3. A comparison of autocorrelations for the shuffling algorithm and the random number generator.

To compare this shuffling algorithm with a random number generator, we have computed the autocorrelations between the shuffled sequences of 50 numbers and the initial ordinal sequence as a function of the number of shufflings. Similarly, we also computed the autocorrelations between the first, second, and succeeding sequences with the first sequence of 50 random numbers generated by the built-in RNG in our computer (a HP-730 workstation). Figure 3 suggests that sequences of random numbers generated by the shuffling algorithm are as random as those obtained by the RNG, even when we employ only seven riffle shuffles.

To compare performance in speed, we have monitored the CPU time required by both techniques and find that the riffle shuffle is approximately four times as fast as the RNG. While one might obtain superior randomness with specifically developed, "portable" RNGs, it is not evident to us that speed would be improved, a matter which may be worthy of further study.

While it turns out that speed of the packing algorithm is not highly important for the large-strain simulations of the present study, it would be crucial to the investigation of the effects of packing parameters on the small-strain properties and the stability of sphere packings [26].

B. *Filling Microcells*

In our packing algorithm the size of a microcell is chosen sufficiently small so as to contain the center of not more than one single particle under any circumstance, but also sufficiently large so as to minimize the total number of microcells. For example in 2D, if a rectangular microcell with two sides Δx and Δy is subject to a simple shear, the microcell is deformed into a parallelopiped as illustrated in Fig. 2. If the largest diagonal of the latter is chosen to be equal to the smallest particle diameter, so that no two particles can simultaneously occupy the same microcell during the deformation, we therefore have

$$\Delta y = \frac{d_{\min}}{\sqrt{(\gamma_{\max} + r_{xy})^2 + 1}}, \tag{5}$$

where

$$r = \Delta x / \Delta y, \tag{6}$$

$d_{\min}$ is the smallest particle diameter, and $\gamma_{\max}$ is the shear strain. Usually, the ratio of two sides, is chosen as unity. From the assumed initial density and the known total particle volume, we estimate the size of the simulation cell which is then divided into $nm \times nm$ microcells (Fig. 2), labeled ordinally from 1 to n $(=nm \times nm)$.

To place N particles randomly in the simulation cell, we generate a random sequence of miocrocells by employing the shuffling algorithm described above. We then pick a microcell from the random sequence and place a particle randomly within it, using successive trials when necessary to avoid overlap with previously placed particles, until all N particles are placed successfully. Figure 4 shows one such random loose-packed configuration for 132 disks.

V. THE RELAXATION ALGORITHM AND INITIAL PACKING

In the present mechanics simulation, we utilize the classical (Southwell, [48]) relaxation method to solve Eq. (1). We recall that relaxation, an iterative method, involves two procedures to accelerate convergence. First, the relaxation order is determined by searching for the residual $(\delta_i)_{\max}$ (the difference between the right-hand and left-hand scalar components of Eq. (1), evaluated at the current value of $\mathbf{x}$ in a given iteration), of greatest magnitude $|\delta_i|$ then "relaxing" the corresponding equation by calculating a new value $\mathbf{x}$ such that $(\delta_i)_{\max} = 0$.

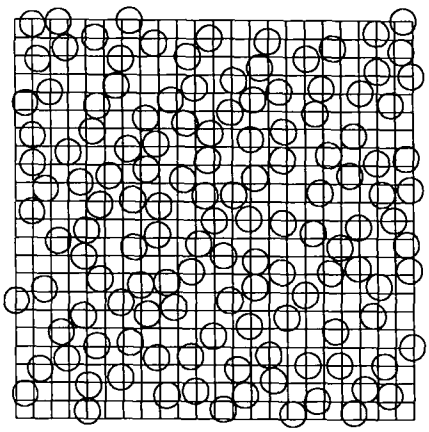

FIG. 4. Random loose-packed configuration for 132 disks (density = 0.43).

This modifies all other residuals, which also depend on $\mathbf{x}$. Next, we employ a rapidly converging relaxation mode that alters only that element x_j of $\mathbf{x}$ having coefficient K_{ij} with the largest absolute magnitude $|K_{ij}|$. The procedure is applied repetitively until all the residuals satisfy a preset convergence criterion on some norm $\|\delta\|$ (in our calculations, the standard Euclidean norm). The fluctuations thus determined serve to move only those particles, or particle clusters, having nonequilibrated forces or moments. Hence, the centroids of isolated clusters do not fluctuate, and we avoid the singularity in Eq. (1). We believe, incidentally, that such a technique might be useful in various types of percolation problem.

The relaxation method is particularly effective for the initial mechanical packing, since in the early stages, the number of particle contacts is small, and only those particles not in equilibrium need be moved. Furthermore, relaxation always eliminates the maximum unbalanced force by making the minimal adjustment of particle configuration.

For both the packing stage and the subsequent deformation, the (Cauchy) stress tensor for the assemblage is computed from the standard quasi-static formula, given, e.g., by Bashir and Goddard [9]. After randomly placing N particles in the simulation cell, we impose a cyclic shearing deformation (static "jiggling") on the system and simultaneously maintain an isotropic confining pressure (as a numerical control on the trace of the stress tensor). During compaction the particles are treated generally as frictionless, so that contacts slide freely and the system densifies more quickly. Cyclic deformation further destroys load-bearing granular chains and speeds up densification. Our packing algorithm appears capable of bringing an initially loose configuration to a random dense state having any desired feasible density. Figure 5 shows one such 2D random dense-packed system.

To provide some test of initial randomness, the radial distribution functions $g(r)$ for the monodisperse assemblages have been computed and compared with those generated by the Percus–Yevick (P-Y) equation of statistical mechanics and by

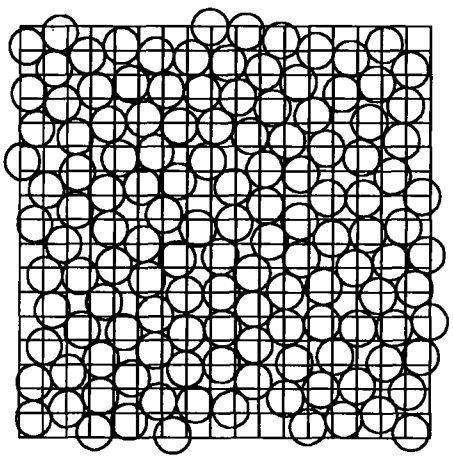

FIG. 5. Random dense-packed configuration for 132 disks (density = 0.80).

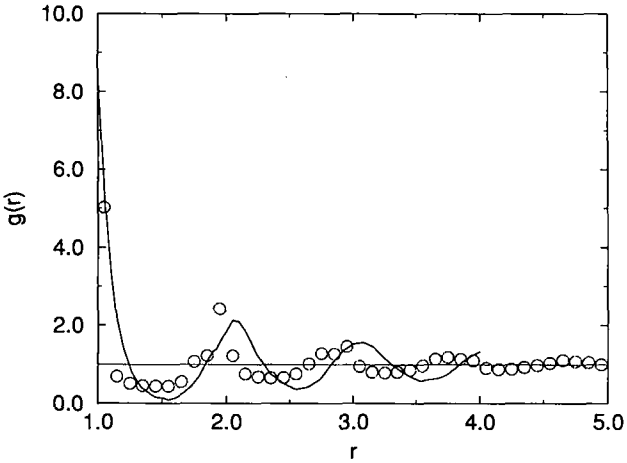

FIG. 7. The simulated radial distribution function for 2D dense-packed configurations of 132 disks (discrete points), compared with the M-C radial distribution function (solid curve).

a Monte Carlo (M-C) simulation [52, 54, 56]. Figure 6 shows the smoothed (i.e., average) $g(r)$ distribution function for 100 realizations of an initially loose-packed configuration of 132 disks (density = 0.43). Figure 7 shows the $g(r)$ for 100 realizations of dense-packed configurations of 132 disks (density = 0.80, close to those for 2D random dense packing). For 3D, Fig. 8 shows the $g(r)$ for 30 realizations of loose-packed configurations of 132 spheres (density = 0.27). Finally, Fig. 9 shows $g(r)$ for 10 realizations of moderately dense-packed configurations of 90 spheres (density = 0.58). We note a weak split second peak, reminiscent of Finney's [25] experimentally determined radial distribution function for a dense packing of 8000 steel balls, where we recall, however, that gravity may play some role.

VI. GRANULAR CONDUCTIVITY

To relate scalar conductivity to granular fabric, we review briefly the underlying theory and the mean-field approximation of Batchelor and O'Brien [10]. We consider a simplified two-phase medium, with the continuous phase or "matrix" having relatively small conductivity, such as a packed bed of steel balls with air filling the interstitial void. We use notation appropriate to electrical conduction in the following discussion, with ϕ denoting electrical potential. The mean potential gradient will be written as $\langle \nabla \phi \rangle$, where $\nabla \phi$ is the local electrical potential gradient in the medium and the brackets $\langle\ \rangle$ denote a volume average over the medium. The local current density $\mathbf{J}$ is equal to $-k_0 \nabla \phi$ at a point in the matrix and $-k_p \nabla \phi$ at a point in a

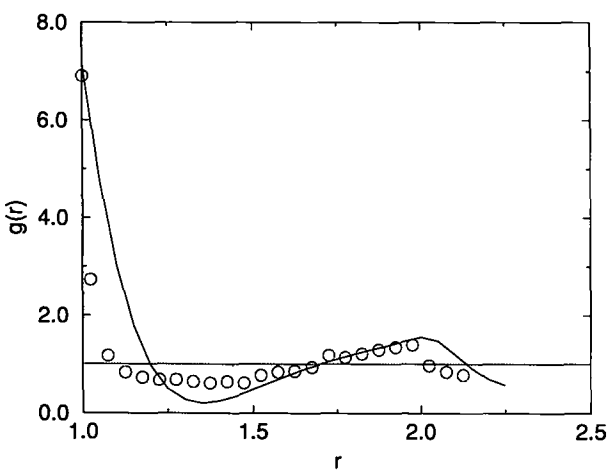

FIG. 6. The simulated radial distribution function for 2D loose-packed configurations of 132 disks (discrete points), compared with the P-Y radial distribution function (solid curve).

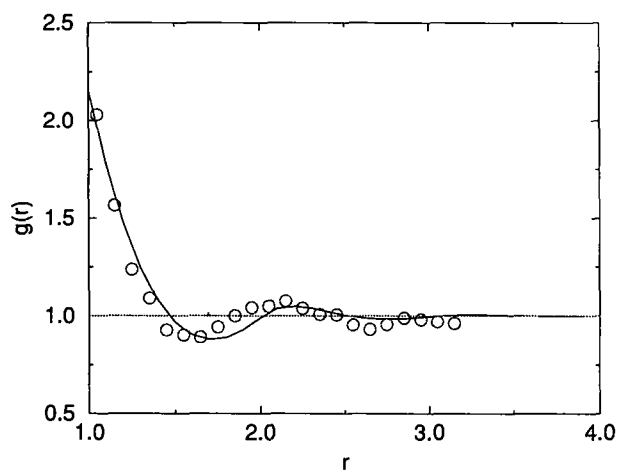

FIG. 8. The simulated radial distribution function for 3D loose-packed configurations of 132 spheres (discrete points), compared with the P-Y radial distribution function (solid curve).

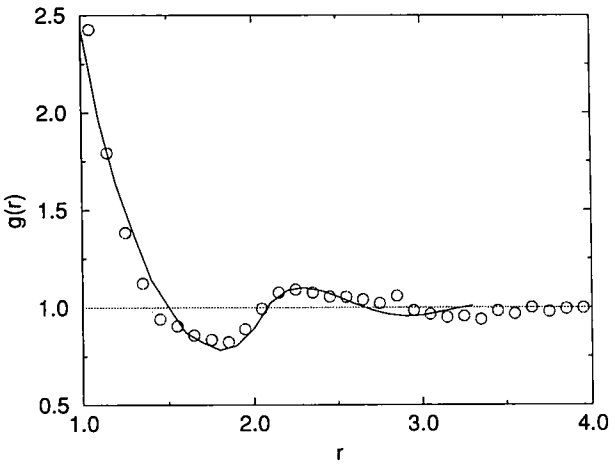

FIG. 9. The simulated radial distribution function for 3D moderately dense-packed configurations of 90 spheres (discrete points), compared with the P-Y radial distribution function (solid curve).

particle. At each point on the surface of a particle, the potential ϕ and the normal component of $\mathbf{J}$ are continuous, and at each interior point in the particles or matrix,

$$\nabla \cdot \mathbf{J} = 0, \quad \nabla^2 \phi = 0. \tag{7}$$

Because of the intrinsic linearity, the magnitudes of all potential differences are proportional to $\langle \nabla \phi \rangle$, and so for the mean flux we have the linear relation [10]

$$\langle \mathbf{J} \rangle = -\mathbf{K}^* \langle \nabla \phi \rangle, \tag{8}$$

where the effective conductivity $\mathbf{K}^*$ is a second-rank tensor, dependent on the structure of the medium and where, by definition, we have

$$\langle \mathbf{J} \rangle = \frac{1}{V} \int_V \mathbf{J} dV = \frac{1}{V} \int_{V_m} \mathbf{J} dV + \frac{1}{V} \sum^N \int_{V_p} \mathbf{J} dV, \tag{9}$$

where V, V_p, and V_m represent the volumes of the entire medium, the individual particles, and the matrix phase, respectively, and N is the number of particles. In the limit of a nonconductive matrix ($k_0 \to 0$), the first term on the right-hand side of Eq. (9) vanishes, so that

$$\langle \mathbf{J} \rangle = \frac{1}{V} \sum^N \int_{V_p} \mathbf{J} dV. \tag{10}$$

On application of Eq. (7) and the Gauss divergence theorem to Eq. (10) (with $\nabla \cdot \mathbf{xJ} = \mathbf{J} + \mathbf{x}\nabla \cdot \mathbf{J}$), one obtains

$$\langle \mathbf{J} \rangle = \frac{1}{V} \sum^N \int_{S_p} \mathbf{xJ} \cdot \mathbf{n} dS, \tag{11}$$

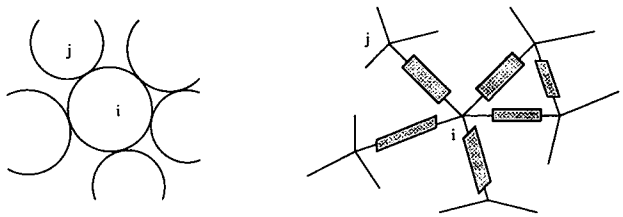

FIG. 10. Particle assemblage and equivalent resistor network.

where S_p denotes the surface of a particle, $\mathbf{x}$ is the spatial position on S_p, and $\mathbf{n}$ is the unit outer normal to S_p. Noting that the term $\mathbf{J} \cdot \mathbf{n} dS$ represents current passing through the portion dS of S_p and assuming [10] that the current is localized at discrete points of particle contact, one further obtains

$$\langle \mathbf{J} \rangle = \frac{1}{V} \sum^N \sum^C \mathbf{x}_c Q_c, \tag{12}$$

where Q_c is current flowing through the contact point c for a given particle p and C is the number of distinct contacts among the N particles. With the assumption of localized current, the assemblage becomes equivalent to the random resistor network illustrated in Fig. 10. Furthermore, for spherical particles, $\mathbf{x}_c = \mathbf{x}_p + R_p \mathbf{n}$, where $\mathbf{x}_p$ is the particle centroid, and Eq. (12) becomes

$$\langle \mathbf{J} \rangle = \frac{1}{V} \sum^N R_p \sum^C \mathbf{n}_c Q_c \tag{13}$$

since charge conservation (Kirchhoff's law) gives

$$\sum^C \mathbf{x}_p Q_c = \mathbf{x}_p \sum^C Q_c = 0. \tag{14}$$

We note that the above derivation also yields the stress tensor in a static granular assemblage as a sum of tensor products obtained on replacing Q_c by a contact force vector [19, 21, 39].

As shown by Batchelor and O'Brien [10], one can represent the local interparticle flux Q_c in terms of a local potential difference and an effective contact resistance R_c, which one can obtain for elastic spheres as follows. According to Hertzian theory [37, 34], two linear elastic spheres with radius R in contact will develop a flat contact circle of radius

$$a = \left[\frac{3(1 - \nu^2) f_n R}{4E} \right]^{1/3} \tag{15}$$

under a normal compressive force f_n. Here, E and ν are, respectively, the Young's modulus and Poisson's ratio. For $a \ll R$, the effective resistance for conduction across the contact circle is then given by [10, 30]

$$R_c = 1/2ak_p, \tag{16}$$

where k_p is the conductivity of the particle phase. However, as discussed below, our experimental contact resistance is found to be much larger than Eq. (16), which we believe can be attributed to surface effects such as asperities and oxide films [28, 29, 5, 30].

In order to compute the interparticle current Q_c, the particle potentials ϕ_p must be determined. As in the mechanical counterpart, the local potentials can be additively decomposed into two parts: a "mean-field" contribution derived from the mean potential gradient and a fluctuation ϕ_p' necessary to satisfy the current balance condition within the system. The latter is obtained by solving the system of linear equations of the form of Eq. (1), where, now, **K** represents a conductance matrix, **x** are the potential fluctuations, and **b** is the unbalanced current. The matrix **K** becomes singular when any cluster of particles becomes disconnected from the assemblage, and this singularity is once again resolved by means of the relaxation method.

For the exact numerical solution of the problem we employ Eq. (8) and Eq. (14) to compute the effective conductivity tensor $\mathbf{K}^*$, which we can then compare to the *mean-field* theory [10], in which the potential difference $\phi_j - \phi_i$ between particles i and j is taken to be $(\mathbf{x}_j - \mathbf{x}_i) \cdot \langle \nabla\phi \rangle = -2R\mathbf{n} \cdot \langle \nabla\phi \rangle$, i.e., to the difference in potential at the two sphere centers associated with the mean potential gradient. With this assumption, one no longer has strict local charge conservation, except for certain periodic or "crystalline" arrays.

It is worthwhile to record the special case of a constant contact resistance $\bar{R}_c$, where

$$Q_c = \frac{1}{\bar{R}_c}\Delta\phi = -\frac{2R}{\bar{R}_c}\mathbf{n}_c \cdot \langle \nabla\phi \rangle \tag{17}$$

and where, later, we shall equate $\bar{R}_c$ with an appropriate average

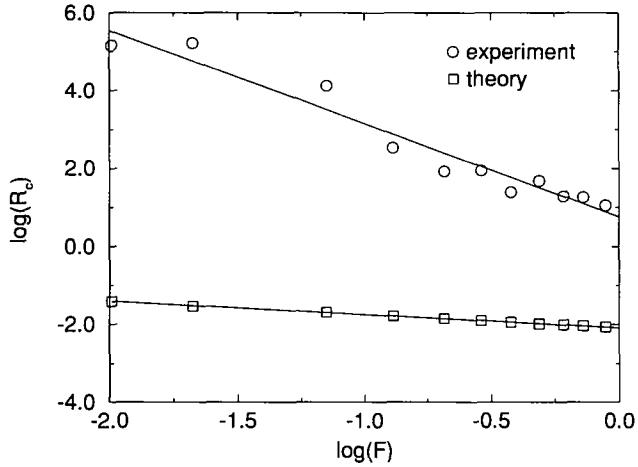

FIG. 11. Comparison of the experimentally measured contact resistance vs. load with the theoretical prediction for Hertzian contact.

of course, readily modify the above calculation to allow for local variations in R_c and R_p, as actually done in all our numerical computations, for which we again recall the computer program listing is given by Zhuang [57].

Faced at one stage in our study with an extremely large discrepancy between the experimentally measured conductivity and numerical simulations based on Eqs. (15)–(16), we were forced to conduct an experiment to determine the electrical contact resistance between balls as a function of normal load. The relationship between resistance and load, as the average of seven experiments, is plotted in Fig. 11, where the predictions from Eqs. (15)–(16) are shown for comparison. The overall scatter in the experimental data is within 20% of the average. The relatively large scatter can probably be ascribed to the nonuniformity of the ball surfaces and associated contaminant

(Coulomb) interparticle friction, nonlinear contact mechanics, and initial packing density on the mechanical behavior. Of particular interest is the Reynolds dilatancy, shear strength, and evolution of the granular microstructure. Simulations of the standard "triaxial" (i.e., symmetric uniaxial) compression of soil mechanics were conducted to explore the effects of the initial density on mechanical behavior as well as on scalar transport properties. For this special deformation, a brief exploration was made of the effects of number of particles N per periodic cell. (Because of memory limitations on our workstation, we were forced to employ a supercomputer for this purpose.) The computations show only a small change, a fraction of a percent, in computed stresses at different strains, for N ranging between 48 and 200. The mechanical simulations are discussed next while the transport properties are covered below. All simulation results presented here are obtained as ensemble averages over five realizations of initial random packings with specified density.

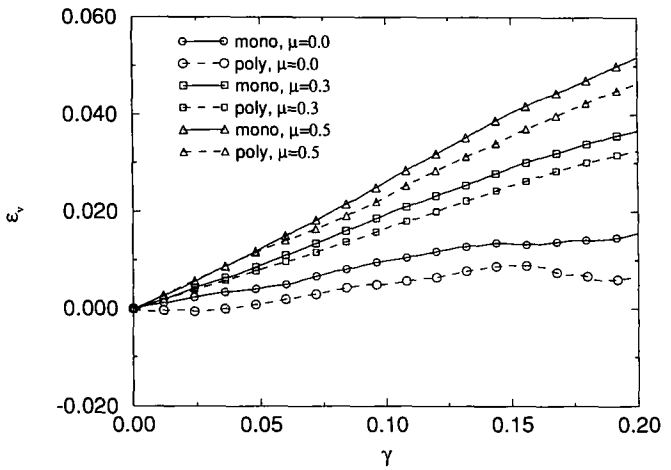

FIG. 12. Effect of interparticle friction on dilatancy of 3D assemblages in simple shear. (γ denotes shear strain and $\varepsilon_v = \ln V/V_0$, where V_0 and V refer to initial and current volumes, respectively.)

A. *Effect of Interparticle Friction*

This study involves both 2D and 3D mono- and poly-disperse assemblages subject to simple shearing under constant mean pressure. The main purpose of the 2D simulations was to compare against the prior results of Bashir and Goddard [9]. The 2D assemblages consist of 132 disks initially packed to random dense packing of about 0.82 area fraction. The 3D granular assemblages contain 48 spheres, initially packed to an approximate dense random packing with volume fraction 0.60. By a scaling based on contact stiffness and particle radius, one can specify an externally imposed nondimensional pressure pR/k_n, where p, k_n, and R denote, respectively, the confining pressure, normal stiffness, and particle radius under which interparticle overlap (proportional to normal force) will not exceed about 0.1% of particle radius, which is a nominal representation of "nearly rigid" particles [9]. This pressure, estimated to be 6.0×10^{-5} for 2D and 4.0×10^{-5} for 3D, is employed during initial packing and subsequent shearing. Both the 2D or 3D test assemblages are subjected to simple shear, up to 20% strain, with different interparticle friction coefficients under otherwise identical conditions. In what follows, we present only the simulation results for 3D assemblages; the results for 2D, which generally confirm the previous work [9], can be found in Zhuang [57].

The nondimensional particle radii are taken as unity by definition for monodisperse systems and as 0.8, 1, and 1.25, respectively, in the polydisperse systems, which are assigned approximately the same total volume of particles of the three different sizes. In particular, we use 27 spheres of radius 0.8, 14 spheres of radius unity, and 7 spheres of radius 1.25. Nondimensional normal and shear contact stiffnesses are taken as $k_n = 1$ and $k_t = 0.8$, respectively. To clarify the influence of particle friction on Reynolds dilatancy and yield strength of randomly dense-packed assemblages, we have carried out several simulations on mono- as well as poly-disperse assemblages, with sliding friction coefficients $\mu = 0$, 0.3, and 0.5, respectively.

The following conclusions can be drawn from the results presented in Figs. 12 and 13: Dilatancy increases with increasing μ, even at the inception of shearing, in agreement with many previous results [20, 12, 16], including those for (the 2D) polydisperse systems of Bashir and Goddard [9], a finding which is contrary to the classical Reynolds hypothesis for dense sphere assemblages. The stress ratio $(\sigma_1 - \sigma_3)/p$, where σ_1, σ_3, and p are major, minor, and mean compressive stress, also increases with increasing magnitude of μ. Polydispersity is seen to have a noticeable effect.

From Fig. 14, one sees that the coordination number Z, say, decreases drastically in the start of shearing, usually within first 1% strain, indicating that significant particle rearrangement

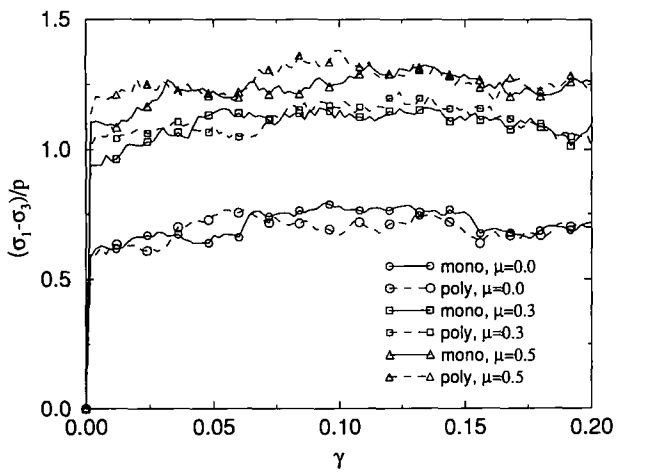

FIG. 13. Effect of interparticle friction on yield strength of 3D assemblages in simple shear.

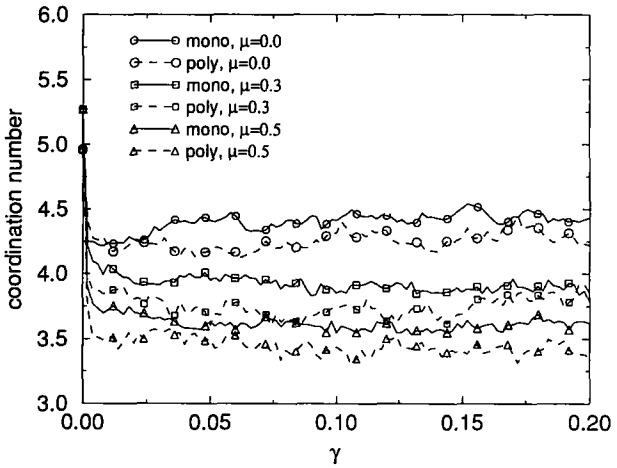

FIG. 14. Effect of interparticle friction on average coordination number of 3D assemblages in simple shear.

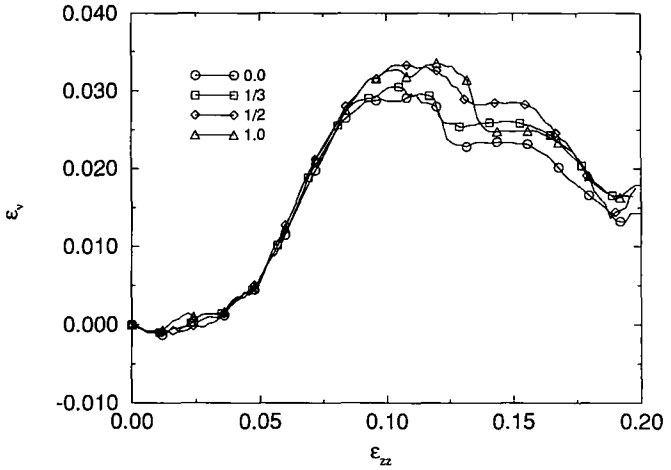

FIG. 15. Effect of contact nonlinearity on dilatancy of 3D assemblages in triaxial compression. (ε_{zz} denotes the axial strain.)

takes place early in the deformation [36, 42]. The value of Z then fluctuates about a roughly constant level throughout the subsequent deformation [12]. Higher interparticle friction generally results in lower final Z values. Although Z varies with shear strain and interparticle friction, it is found always to be greater than the critical coordination number $Z_c \approx d/(d-1)$ for geometric percolation in the spatial dimension $d > 1$ [26, 47].

The ratio $f = Z/Z_{max}$ represents the fraction of active contacts or "bonds" in the network of particle contacts relative to that of the densest possible systems, with Z_{max} equal to 6 for 2D triangular lattices and to 12 for 3D FCC lattices [26]. The computed values of f lie between the geometric and central-force elastic-percolation thresholds [26]. By contrast, we recall that the previous 2D simulations [9] gave asymptotic, large strain f values very close to the geometric percolation threshold (which is much smaller than that for central-force elastic percolation [26]).

Based on detailed microscopic observations we find, as points of general qualitative agreement with several previous studies, that: (1) granular microstructure generally evolves such that contact normals concentrate in the direction of major principal stress during deformation [49]; (2) the assemblage is composed of two types of region; a skeleton composed of oriented, heavily stressed chains of particles, together with amorphous, less stressed regions surrounding this skeleton, where most of the breaking and making of contacts occurs while the skeleton remaining relatively unaltered for small incremental deformations; (3) particle rolling is the major deformation mechanism, increasingly so as interparticle friction increases [43].

B. *Effect of Nonlinear Contact*

Since the linear-elastic contact model offers computational simplicity, while providing useful qualitative insights into the link between micromechanical macroscopic properties [11, 12, 20–22, 51] and since we are mainly interested in the ideal rigid particle limit, most of our simulations are carried out for this model. However, we felt it important to explore the effects of nonlinearity and for this purpose we have investigated a simple nonlinear contact model given by the power-law for elastic stiffness

$$k_n = Cf_n^{\lambda} \tag{21}$$

where C is a material constant and f_n is normal load, with $\lambda = \frac{1}{3}$ corresponding to Hertzian contact.

A monodisperse system with 48 spheres packed to initial density $\phi = 0.60$ and with $\mu = 0.15$ is subjected to triaxial compression under a constant mean confining pressure $p = 4 \times 10^{-5}$. Values of the exponent in Eq. (21), $\lambda = 0, \frac{1}{3}, \frac{1}{2}$, and 1 were explored, with 0 representing the linear contact and 1 representing the strongest nonlinearity. As before, the tangential stiffness k_t is simply taken to be $0.8k_n$.

From Fig. 15 one sees that contact nonlinearity has but little influence on dilatancy in the small- to intermediate-strain region, although some effects are observed at higher compressions. Moreover, it is found [57] that the average number of particle contacts is not strongly affected. One might expect that the nonlinear contact law would tend to make strong contacts (in terms of contact force) stronger and weak contacts weaker, therefore influencing the contact-force distribution. However, although we do indeed observe variations in force distribution, the different degrees of nonlinearity are found to yield only a small deviation in the average normal force [57]. Finally, from Fig. 16, one sees that the strength of the assemblage tends to increase somewhat with extreme nonlinearity. Otherwise, the generally small effect of contact nonlinearity suggests to us that complicated nonlinear elastic contact laws are not strictly necessary for modeling many aspects of the granular mechanics.

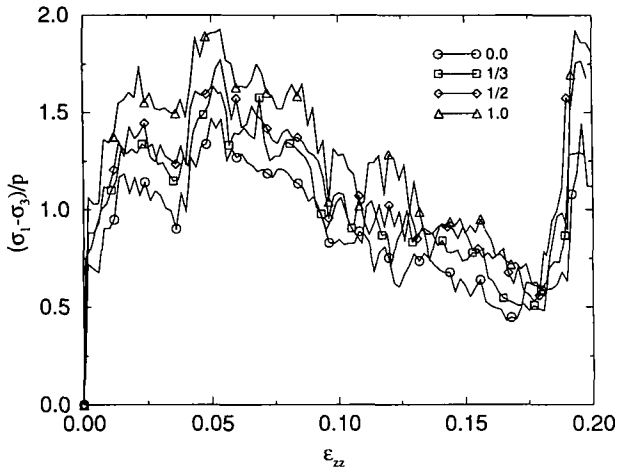

FIG. 16. Effect of contact nonlinearity on strength of 3D assemblages in triaxial compression.

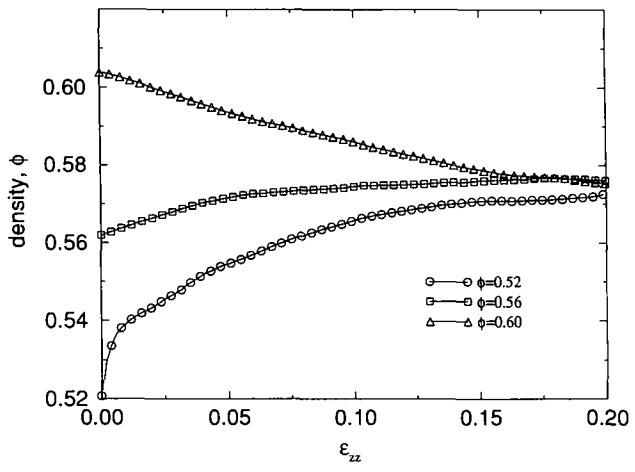

FIG. 18. Effect of initial density on density evolution of 3D assemblages in triaxial compression.

C. *Effect of Initial Specimen Density*

To simulate the influence of the initial void ratio or packing density on the mechanical and electrical conductivity, we have generated three random monodisperse packings of 100 spheres, with different initial densities, 0.52, 0.56, and 0.60, respectively. The friction coefficient μ is taken to be 0.15, corresponding to measurements on steel ball bearings discussed below. All three packings are subjected to triaxial compression under nondimensional confining stress $\sigma_2 = \sigma_3 = 4 \times 10^{-5}$ normal to the $\phi = 0.60$, exhibits positive dilatancy from the very beginning of the deformation. Nevertheless, the densities of three systems, either contracting or expanding, tend to approach the same "critical-state" [24] value asymptotically.

Figure 19 shows that for loose systems the shear strength increases monotonically. However, for the initially dense system its strength increases first, until a peak value is reached; then it decreases. Similar observations in real triaxial compression tests are discussed below. Again, both the loose and dense

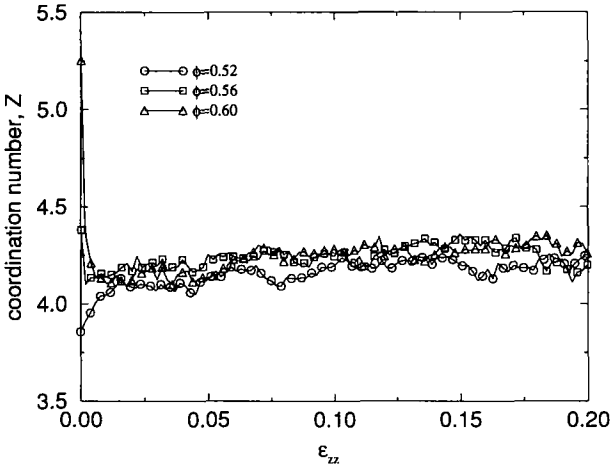

FIG. 20. Effect of initial density on coordination number of 3D assemblages in triaxial compression.

strain and then exhibit fluctuating, slightly increasing values (Fig. 20).

As an attempt to elucidate these observations, we note that in a loose system the initial number of interparticle contacts and, hence, the coordination number are low, just exceeding the elastic percolation threshold (at which there just begin to exist sample-spanning chains of frictionless particles capable of supporting an ambient shear stress [26]). However, owing to the lack of sufficient contact force from neighboring particles, load bearing chains are highly unstable to Euler buckling such that a given particle chain will generally undergo a kind of lateral "branching" until it becomes capable of supporting increased axial compressive stress [26]. Therefore, the overall granular structure is less stable and more likely to collapse to a more stable, denser system upon deformation and thereby to generate load-bearing capability. Such capability is further enhanced as the system becomes more dense. On the other hand, the dense system must expand in order to deform and, hence, loses contacts initially. Owing to the volume expansion against the ambient pressure, the system exhibits shear strength, but further dilatancy reduces the system density and decreases the stability of the granular chain structure and the ability to support the external loads. This explains the after-peak strength loss for dense systems illustrated by Fig. 19, which is known to be a feature of many real granular media [24].

VIII. ELECTRICAL CONDUCTIVITY

A. *Numerical Simulations*

For the purpose of comparison to our experiments, the computer code is modified specifically to simulate triaxial compression, for an assemblage having the physical properties in Table I and with the experimental loading conditions as input parameters. The stress and electrical conductivity are computed simultaneously.

TABLE I

The Physical Properties of the Steel Balls Employed in the Experiments

Diameter (m)	0.00278 ± 0.00000064
Density (kg/m^3)	0.007667
Elastic modulus (MPa)	1.999×10^4
Poisson's ratio	0.29
Friction coefficient	0.15
Electrical conductivity (ohm · m)$^{-1}$	166.7

The computed nondimensional normal forces are converted to actual forces by a scaling based on the particle radius and ambient confining pressure so that the contact resistance between two particles can be compared to the experimentally determined load–resistance relation of Fig. 11. Any effects of tangential force on contact resistance are neglected.

Turning to the axial conductivity K_{zz}, we see from Figs. 19 and 21 the similarity between the behavior of shear strength and conductivity, although there is more fluctuation in conductivity than in strength. For the initially dense system, with $\phi = 0.60$, the conductivity increases to a peak within the first 2% of axial strain; then it fluctuates widely in a decreasing trend.

Upon compression, load-bearing chains are built up gradually in the axial (z) direction creating more conductive pathways for current. Therefore, in early stages of deformation, the conductivity increases steadily despite the fact that system experiences a loss in the total number of contacts (see Fig. 14), mainly in the x–y plane [57], the direction of minor principal stress. Owing to the dilatancy of the system (Fig. 17), these granular chains become progressively less stable. When the system is further expanded, these load-bearing chains finally buckle. The branching-out of chains diverts current from the preferred axial direction. Therefore, one observes an after-peak decrease in

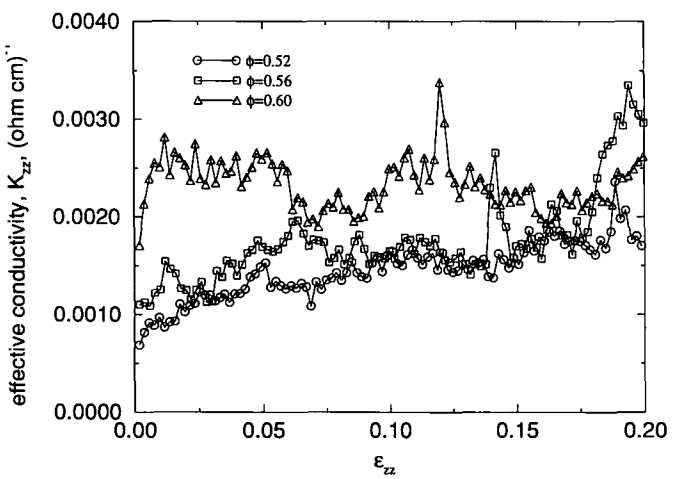

FIG. 21. Dependence of axial conductivity on axial strain and initial density ϕ.

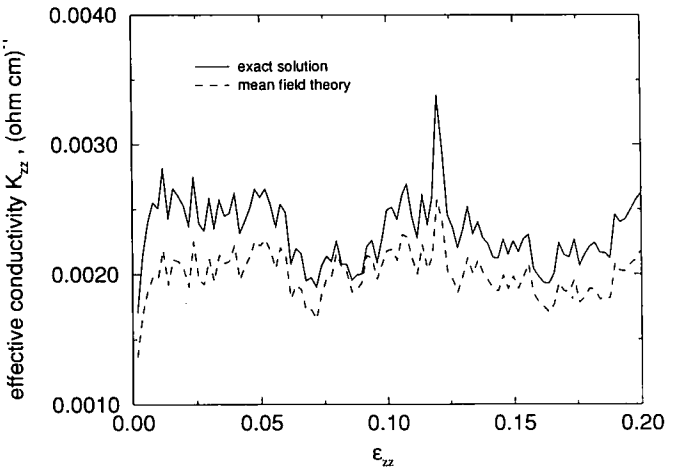

FIG. 22. Comparison between the exact numerical solution and mean field theory for effective conductivity of monodisperse assemblages (initial $\phi = 0.60$).

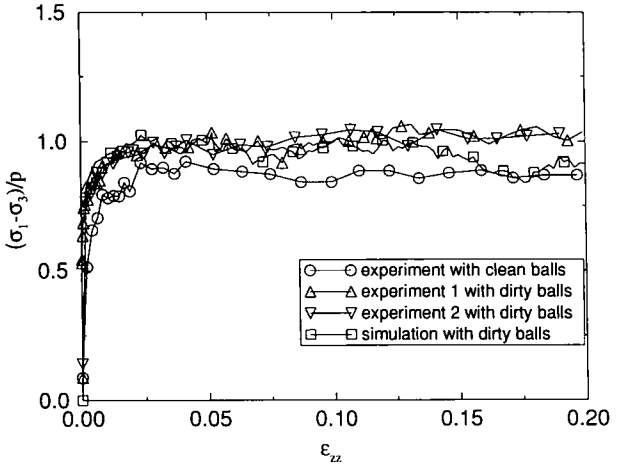

FIG. 23. Comparison of shear strength between numerical simulation and experiments with dirty balls (initial $\phi = 0.60$).

conductivity. The subsequent buildup and buckling of new, heavily stressed chains is the primary cause of the fluctuations in conductivity. On the other hand, the densification in the loose systems during the deformation tends to stabilize these progressively loaded chains, thus resulting in a steady increase of conductivity.

The results shown in Fig. 22 are obtained from Eq. (13), with $\overline{R}_c$ being taken as the number average of all the computed individual contact resistances. If instead, $\overline{R}_c$ is based on the resistance evaluated at the average normal contact force, then Eq. (13) overpredicts by roughly the same amount, with the fluctuation pattern being the same. Thus, the mean field theory of Batchelor and O'Brien can obviously be used to great advantage for a qualitative understanding of scalar transport and the elucidation of granular fabric.

IX. COMPARISON TO EXPERIMENTS AND CONCLUSIONS

Three triaxial compression tests have been carried out, one with nominally clean balls and two with nominally dirty balls, at approximately $\phi = 0.60$ as the initial density. Here, "clean" refers to the balls from which any protective oil film was removed with acetone and which are expected to have relatively little surface contamination. Unfortunately, however, the normal load–contact resistance relation was not experimentally determined immediately after the cleaning process. "Dirty" refers to balls, which were exposed to the laboratory air for approximately four months after cleaning with acetone, which are expected to possess an insulating oxide film (or high contact resistance) and for which the load–contact resistance relation (Fig. 11) and the interparticle friction coefficient were subsequently measured. The experimental results for clean balls are given here solely for the comparison with the dirty balls [57].

Figures 23 and 24 indicate that the numerical simulation and physical experiments on dirty balls are in qualitative agreement. Comparison of the experimental results for clean and dirty balls in Fig. 24 also reveals that the individual contact resistances can drastically affect the overall conductivity.

In summary, the results of the present investigation show that: (1) interparticle friction has great influence on Reynolds dilatancy for random dense-packed granular assemblages, both mono- as well as poly-disperse, a result that is contrary to Reynolds' original hypothesis [44]; (2) the use of linear contact mechanics is justified near the ideal rigid-particle limit; and (3) scalar transport properties such as electrical conductivity can serve as good indicators of microstructural anisotropy and particle–contact topology, even when electrical contact resistance deviates greatly from the Hertzian contact prediction.

APPENDIX I: BASIC EQUATIONS AND THE STIFFNESS MATRIX

During the deformation of granular assemblages, particles move with independent degrees of freedom and interact with each other only at their contact points. The assumed force–displacement relationship is presented here for the case of two spherical particles A and B in contact, as shown in Fig. 25.

The particle radius is denoted by R and its centroid by $\mathbf{X}$. Upon the deformation, a particle undergoes infinitesimal increments of translation and rotation $\mathbf{u}$ and $\boldsymbol{\omega}$, respectively. The superscripts in Fig. 25 and in the sequel denote a given particle. The unit contact normal to the tangential plane is $\mathbf{n} = (\mathbf{X}^B - \mathbf{X}^A)/|\mathbf{X}^B - \mathbf{X}^A|$. The interaction between the particles depends on the relative motion of the contact points, with components of relative displacement in the normal and tangential directions given, respectively, as

$$\Delta\mathbf{u}_n = (\mathbf{u}^B - \mathbf{u}^A) \cdot \mathbf{nn} \tag{22}$$

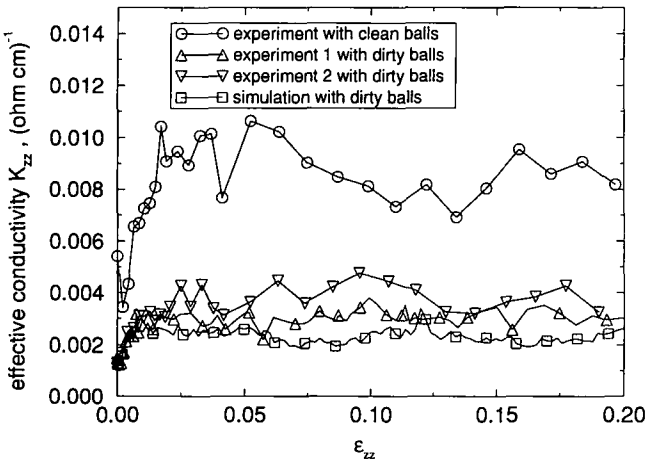

FIG. 24. Comparison of electrical conductivity between numerical simulation and experiments with dirty balls (initial $\phi = 0.60$).

and

$$\Delta\mathbf{u}_t = (\mathbf{u}^B - \mathbf{u}^A) - \Delta\mathbf{u}_n + \mathbf{R}^B \times \boldsymbol{\omega}^B + \mathbf{R}^A \times \boldsymbol{\omega}^A, \quad (23)$$

where $\mathbf{u}^{AB} = \mathbf{u}^B - \mathbf{u}^A$, $\mathbf{R}^A = R^A\mathbf{n}$, and $\mathbf{R}^B = R^B\mathbf{n}$.

These relative displacements are used to calculate increments of normal and shear forces, $\Delta\mathbf{f}_n$ and $\Delta\mathbf{f}_t$, according to

$$\Delta\mathbf{f}_n = k_n \Delta\mathbf{u}_n \quad (24)$$

and

$$\Delta\mathbf{f}_t = k_t \Delta\mathbf{u}_t, \quad (25)$$

where k_n and k_t denote the normal and tangential elastic stiffnesses, respectively, which may be allowed to depend on $\Delta\mathbf{f}_n$ and $\Delta\mathbf{f}_t$.

Furthermore, the force increments $\Delta\mathbf{f}_n$ and $\Delta\mathbf{f}_t$ are added, respectively, to the initial forces $\mathbf{f}_n^0$ and $\mathbf{f}_t^0$ to between particles yield the current values:

$$\mathbf{f}_n = \mathbf{f}_n^0 + \Delta\mathbf{f}_n \quad (26)$$

and

$$\mathbf{f}_t = \mathbf{f}_t^0 + \Delta\mathbf{f}_t. \quad (27)$$

The normal and tangential components, $\mathbf{f}_n = f_n\mathbf{n}$ and $\mathbf{f}_t = \mathbf{f} - \mathbf{f}_n$, of the force vector are both set to be zero if f_n is not compressional (since cohesionless particles cannot sustain tensile force). A (Coulomb) sliding friction law is incorporated as follows: the magnitude of the shear force $\mathbf{f}_t$ given by Eq. (27) is checked against the maximum possible shear force magnitude,

$$(f_t)_{\max} = \mu|\mathbf{f}_n|, \quad (28)$$

where $\mu(\equiv\tan\phi_\mu)$ is the coefficient of sliding friction (defining the so-called angle of intergranular friction ϕ_μ). If $|\mathbf{f}_t|$ exceeds $(f_t)_{\max}$, sliding occurs at the contact point. Under this circumstance, $\mathbf{f}_t$ takes the value of $(f_t)_{\max}$, and maintains its direction. Therefore, the total force and couple exerted on particle A by particle B are given by

$$\mathbf{f} = \mathbf{f}_n + \mathbf{f}_t \quad (29)$$

$$\mathbf{M} = \mathbf{R}^A \times \mathbf{f}_t. \quad (30)$$

These are next decomposed into three Cartesian components, yielding

$$\mathbf{F} = \mathbf{F}^0 + \mathbf{k}_{AB}\,\Delta\mathbf{u}(AB), \quad (31)$$

where, $\mathbf{F} = [f_x, f_y, f_z, m_x, m_y, m_z]$, the generalized force, represents the components of force and moment exerted currently on particle A by B. $\mathbf{F}^0 = [f_x^0, f_y^0, f_z^0, m_x^0, m_y^0, m_z^0]$ represents the components of force and moment in the previous state. The matrix $\mathbf{k}_{AB}$ is the local contact–stiffness matrix, while $\Delta\mathbf{u}(AB)$ is the generalized relative displacement between A and B,

$$\Delta\mathbf{u}(AB) \equiv \begin{pmatrix} u_x^B - u_x^A \\ u_y^B - u_y^A \\ u_z^B - u_z^A \\ R^B\omega_x^B + R^A\omega_x^A \\ R^B\omega_y^B + R^A\omega_y^A \\ R^B\omega_z^B + R^A\omega_z^A \end{pmatrix}, \quad (32)$$

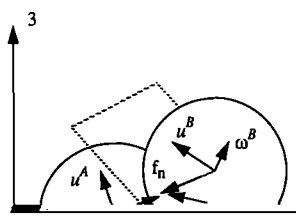

$$\sum_B \mathbf{F} = \sum_B \mathbf{F}^0 + \sum_B \mathbf{k}_{AB}\,\Delta\mathbf{u}(AB) = \mathbf{0} \tag{33}$$

or

$$\sum_B \mathbf{k}_{AB}\,\Delta\mathbf{u}(AB) = -\sum_B \mathbf{F}^0. \tag{34}$$

In the current simulation, the displacement of each particle is additively decomposed into two components: the macroscopically imposed mean $\bar{\mathbf{u}}$ defined by the global velocity gradient and a fluctuation $\mathbf{u}'$, the latter being such that the force balance equation (34) is satisfied. Therefore, Eq. (34) becomes

$$\sum_B \mathbf{k}_{AB}\,\Delta\mathbf{u}'(AB) = -\sum_B \mathbf{F}^0 - \sum_B \mathbf{k}_{AB}\,\Delta\bar{\mathbf{u}}(AB) \tag{35}$$

for $A = 1, 2, \ldots, N$, with N denoting the total number of particles within the system. This leads in an obvious way to a system of quasi-linear equation (1) for the $(6N)$ fluctuations, where $\mathbf{x} = [u_x'(1), u_y'(1), u_z'(1), \omega_x'(1), \omega_y'(1), \omega_z'(1), \ldots, u_x'(N), u_y'(N), u_z'(N), \omega_x'(N), \omega_y'(N), \omega_z'(N)]$ is the vector of the fluctuating displacements and rotations and $\mathbf{b}$ is the unbalanced force arising from the displacements from the prior iteration.

ACKNOWLEDGMENTS

This work has been partially supported by the United States Air Force Office of Scientific Research under Grant No. AFOSR 49620-92-J-0037. Mr. Steve Porter deserves much credit for his excellent help in design of the experimental apparatus.

REFERENCES

1. T. K. Agarwal and I. Ishibashi, "Anisotropic Elastic Constants of Granular Assembly from Wave Velocity measurements," in *Advances in Micromechanics of Granular Materials*, edited by H. H. Shen *et al.* (Elsevier, Amsterdam, 1992), p. 51.
2. M. P. Allen and D. J. Tildesley, *Computer Simulation of Liquids* (Clarendon, Oxford, 1987).
3. A. Anandarajah, Ph.D. dissertation, University of California, Davis, 1982 (unpublished).
4. A. Anandarajah, K. Sobhan, and N. Kuganenthira, "Fabric Anisotropy and Incremental Stress–Strain Behavior of Soils," in *Proceedings, 2nd International Conference on Discrete Element Methods, 1993*, edited by J. R. Williams and G. G. W. Mustoe, p. 547.
5. M. Antler, *IEEE Circuits Devices Mag.* **3,** 8 (1987).
6. K. Arulanandan and B. Kutter, "A Directional Structure Index Related to Sand Liquefaction," in *Proceedings, Spec. Conf. Earthquake Eng. Soil Dynamics, ASCE, Pasadena, California, June 19–21, 1978*, p. 213.
7. K. Bagi, *Mech. Mat.* **16,** 101 (1993).
8. J. P. Bardet and J. Proubet, *Comput. Struct.* **39**(3/4), 221 (1991).
9. Y. M. Bashir and J. D. Goddard, *J. Rheol.* **35,** 849 (1991).
10. G. K. Batchelor and R. W. O'Brien, *Proc. R. Soc. London Ser. A* **355,** 313 (1977).
11. R. J. Bathurst and L. Rothenburg, *J. Appl. Mech.* **55,** 17 (1988).
12. R. J. Bathurst and L. Rothenburg, *Mech. Mat.* **9,** 65 (1990).
13. J. G. Berryman, *Phys. Rev. A* **27,** 1053 (1983).
14. R. E. Boltz and G. L. Tuve, *CRC Handbook of the Tables for Applied Engineering Science* (CRC Press, Boca Raton, Florida, 1985).
15. Y-C. Chen, I. Ishibashi, and J. T. Jenkins, *Geotechnique* **38,** 25 (1988).
16. Y-C. Chen, *J. Chinese Inst. Eng.* **13**(2), 147 (1990).
17. C. S. Chang and A. Misra, *Comput. Geotech.* **7,** 269 (1989).
18. C. S. Chang, "Micromechanics Modeling for Deformation and Failure of Granular Material," in *Advances in Micromechanics of Granular Materials*, edited by H. H. Shen *et al.* (Elsevier, Amsterdam, 1992), p. 251.
19. J. Christoffersen, M. M. Mehrabadi, and S. Nemat-Nasser, *J. Appl. Mech.* **48**(2), 339 (1981).
20. P. A. Cundall and O. D. L. Strack, NSF Report, Dept. of Civil and Mineral Eng., University of Minnesota, 1979 (unpublished).
21. P. A. Cundall and O. D. L. Strack, "Modeling of Microscopic Mechanisms in Granular material," in *Mechanics of Granular Materials: New Models and Constitutive Relations*, edited by J. T. Jenkins and M. Satake (Elsevier, Amsterdam, 1983), p. 137.
22. P. A. Cundall, "Computer Simulations of Dense Sphere Assemblies," in *Micromechanics of Granular Materials*, edited by M. Satake and J. T. Jenkins (Elsevier, Amsterdam, 1987), p. 113.
23. P. Diaconis, "Group Representations in Probability and Statistics," (Inst. Math. Statist., Hayward, CA, 1988).
24. J. Feda, *Mechanics of Particulate Materials: The Principles* (Elsevier, Amsterdam, 1982).
25. J. L. Finney, *Proc. R. Soc. London Ser. A* **319,** 479 (1970).
26. J. D. Goddard, *Proc. R. Soc. London Ser. A* **430,** 105 (1990).
27. J. D. Goddard, X. Zhuang, and A. K. Didwania, "Microcell Methods and the Adjacency Matrix in the Simulation of the Mechanics of Granular Media," in *Proceedings, 2nd International Conference on Discrete Element Methods*, edited by J. R. Williams and G. G. W. Mustoe (Intelligent Systems Engineering Laboratory, MIT, Cambridge, MA, 1993), p. 3.
28. J. A. Greenwood and J. B. P. Williamson, *Proc. R. Soc. London Ser. A* **295,** 300 (1966).
29. J. A. Greenwood and J. H. Tripp, *J. Appl. Mech.*, March, p. 153 (1967).
30. R. Holm, *Electric Contacts: Theory and Application* (Springer-Verlag, New York, 1967).
31. I. Ishibashi, Y-C. Chen, and J. T. Jenkins, *Geotechnique* **38,** 25 (1988).
32. J. T. Jenkins and O. D. L. Strack, *Mech. Mat.* **16,** 25 (1993).
33. W. S. Jodrey and E. M. Tory, *Powder Tech.* **30,** 111 (1981).
34. K. L. Johnson, *Contact Mechanics* (Cambridge Univ. Press, Cambridge, UK, 1985).
35. Y. Kishino, "Discrete Model Analysis of Granular Media," in *Micromechanics of Granular Materials*, edited by M. Satake and J. T. Jenkins (Elsevier, Amsterdam, 1987), p. 143.
36. J. Konishi, M. Oda, and S. Nemat-Nasser, "Induced Anisotropy in Assemblies of Oval Cross-Sectional Rods in Biaxial Compression," in *Mechanics of Granular Materials: New Models and Constitutive Relations*, edited by J. T. Jenkins and M. Satake (Elsevier, Amsterdam, 1983), p. 31.
37. R. D. Mindlin and H. Deresiewicz, *J. Appl. Mech.* **20,** 327 (1953).
38. R. J. Mousseau and R. P. Trump, *J. Appl. Phys.* **67** (1967).
39. S. Nemat-Nasser and M. Mehrabadi, "Stress and Fabric in Granular Masses," in *Mechanics of Granular Materials: New Models and Constitutive Relations*, edited by J. T. Jenkins and M. Satake (Elsevier, Amsterdam, 1983), p. 1.
40. S. Nemat-Nasser and B. Balendran, "Micromechanics of Flow and Failure Modes of Particulate Media over a Wide Range of Strain Rates," in

Advances in Micromechanics of Granular Materials, edited by H. H. Shen *et al.* (Elsevier, Amsterdam, 1992), p. 21.

41. M. Oda, *Soils Found.* **12**(1), 17 (1972).
42. M. Oda, *Soils Found.* **12**(2), 1 (1972).
43. M. Oda, J. Konishi, and S. Nemat-Nasser, "Experimental Micromechanical Evaluation of the Strength of Granular Materials: Effect of Particle Rolling, in *Mechanics of Granular Materials: New Models and Constitutive Relations,* edited by J. T. Jenkins and M. Satake (Elsevier, Amsterdam, 1983), p. 137.
44. O. Reynolds, *Philos. Mag.* **20,** 469 (1885).
45. W. Schreiner and K. W. Kratky, *J. Chem. Soc., Faraday Trans. II* **78,** 379 (1982).
46. A. A. Serrano and J. M. Rodriguez-Ortiz, "A Contribution to the Mechanics of Heterogeneous Granular Media," in *Proceedings, Symp. on Plasticity and Soil Mechanics,* Cambridge, 1973."
47. K. S. Shante and S. Kirkpatrick, *Adv. Phys.* **20,** 325 (1971).
48. R. V. Southwell, *Relaxation Methods in Engineering Science* (Oxford Univ. Press, London, 1940).
49. G. Subhash, S. Nemat-Nasser, M. M. Mehrabadi, and H. M. Shodja, *Mech. Mat.* **11,** 87 (1991).
50. C. Thornton and D. J. Barnes, *Acta Mech.* **64,** 46 (1986).
51. J. M. Ting, B. T. Corkum, C. R. Kauffman, and C. Greco, *J. Geotech. Eng. ASCE* **115,** 379 (1989).
52. G. J. Throop and R. J. Bearman, *J. Chem. Phys.* **42,** 2408 (1965).
53. W. T. Tutte, *Graph Theory* (Addison–Wesley, Reading, MA, 1984).
54. Y. Uehara, T. Ree, and F. H. Ree, *J. Chem. Phys.* **70,** 1876 (1979).
55. W. M. Vissher and M. Bolsterli, *Nature* **239,** 504 (1972).
56. W. W. Wood, *J. Chem. Phys.* **52,** 729 (1970).
57. X. Zhuang, Ph.D. dissertation, University of California, San Diego, 1993.